Dual-Polarized Radar Coverage in Terminal Airspaces and Its Effect on Interpretation of Winter Weather Signatures: Current Capabilities and Future Recommendations

HEATHER DAWN REEVES

NOAA/OAR/National Severe Storms Laboratory, and Cooperative Institute for Mesoscale Meteorological Studies, University of Oklahoma, Norman, Oklahoma

JACQUELINE WATERS

National Weather Center Research Experience for Undergraduates, Norman, Oklahoma, and University of Hawai'i at Mānoa, Honolulu, Hawaii

(Manuscript received 4 May 2018, in final form 1 November 2018)

ABSTRACT

This is a feasibility study on the use of dual-polarized radars to infer icing in terminal airspaces (TASs) of commercial airports. The amount and quality of radar coverage in each TAS is quantified as a function of its location, traffic, and vulnerability to icing. No airport has 100% of the TAS covered, but most high-traffic or high-icing airports have comparatively good coverage (between 70% and 90%). A common occurrence during icing is anomalous propagation as 79% of events had an inversion within the TAS. This leads to overestimates in the elevations of icing layers and can cause significant ground-clutter contamination, which can overwhelm the echo produced by precipitation. The effects of beam broadening were also considered. Typical dendrite growth and melting layers can only be resolved in part of the TAS part of the time, or not at all, as these layers are often shallower than the radar beam. Because most airports have coverage from multiple radars, use of a three-dimensional mosaic was investigated. This allows for an increase in the TAS coverage (generally between 5% and 15%) and partly mitigates some of the resolution issues, but the maxima within individual layers are somewhat reduced in the interpolation process. A series of recommendations is made to address the concerns raised by this investigation. These include using only icing tops (not bottoms) to identify areas of icing, use of data mining to retrieve precipitation echo in the presence of ground clutter, and including the beamwidth in radar mosaics.

1. Introduction

This study is motivated by new standards implemented by the Federal Aviation Administration (FAA) that limit the conditions under which commercial aircraft can operate within terminal airspaces (TASs) during winter precipitation. These standards require discrimination between freezing and nonfreezing hydrometeors as well as their size distributions. This may be possible with dual-polarized radars. However, application of radar algorithms to the TAS depends, at a minimum, on the amount and quality of radar coverage, which vary from one TAS to the next. The aim of this study is to quantify the radar coverage within TASs of commercial airports in the continental United States (CONUS) and to assess how the diagnosis of hydrometeor habit is impacted.

In an effort to reduce icing-related accidents, the FAA has instituted new requirements that specify what types of commercial aircraft can depart or land during freezing precipitation [i.e., freezing drizzle (FZDZ) or freezing rain (FZRA)]. Under the new guidelines, some aircraft (especially regional airline types with manual flight control systems) will be prohibited from entering or leaving a TAS if there is any form of freezing precipitation, other aircraft may be certificated to fly in FZDZ but not FZRA, while still others may be certificated to fly in either of these conditions (Cober and Isaac 2012; FAA 2015). Such rules require both hydrometeor classification and size distribution along the proposed flight path. Determining whether sufficient

Corresponding author: Heather Dawn Reeves, heather.reeves@noaa.gov

DOI: 10.1175/JAMC-D-18-0123.1

technology exists to support this requirement is the aim of the Terminal-Area Icing Weather Information for NextGen (TAIWIN; DiVito and Riley 2017) initiative.

The TAS extends from the ground to 3.048 km (10 000 ft) and horizontally by 55.56 km (30 n mi) from the ends of the runways. This is a rather broad area, making it possible for multiple forms of precipitation to occur within a TAS (Crawford and Stewart 1995; Bernstein 2000; Cortinas 2000; Rauber et al. 2000, 2001; Robbins and Cortinas 2002; Changnon 2003; Cortinas et al. 2004; Thériault et al. 2010; Reeves et al. 2014; Elmore et al. 2015; Reeves 2016). While several surface-based observational platforms exist that can be helpful for diagnosing the hydrometeor type and/or size distribution at a single point, the only existing operational network that provides *three-dimensional, within-cloud* observations are radars.

There has been significant development of algorithms for dual-polarized radars to classify the hydrometeor habit during winter precipitation (e.g., Park et al. 2009; Plummer et al. 2010; Hallowell et al. 2013; Serke et al. 2013; Thompson et al. 2014; Ryzhkov et al. 2016; VanDenBroeke et al. 2016). These make use of the spatial distributions and local magnitudes of the radar moments to infer the habit. The drop size distribution can also be determined by applying variational estimation or Bayesian techniques to the radar moments (e.g., Cao et al. 2010, 2013; Yoshikawa et al. 2014). Such advancements suggest there is great promise for the use of dual-polarized radars to meet the new FAA requirements. But, given that only one-third of all commercial airports in the CONUS have a radar within their TAS and increases in beamwidth can degrade radar signatures, it is reasonable to question whether relevant radar signatures are always able to be detected/resolved (e.g., Giangrande and Ryzhkov 2003; Giangrande et al. 2005; Ryzhkov et al. 2005b; Ryzhkov 2007).

Radar coverage and resolution were evaluated for large-hub airports in the United States by Cho (2010). At some of these airports, the coverage and quality were too poor to resolve some weather phenomena. However, the effects on diagnosing icing were not addressed and the study was limited to only large-hub airports. The new restrictions on flight and the recent advancements in dual-polarization provide good incentive to revisit the issue of radar coverage/quality in TASs by the Weather Surveillance Radar-1988 Doppler (WSR-88D) network for all commercial airports in the CONUS.

2. Methodology

The TAS is defined herein as a cylinder with a radius of 55.56 km and depth of 3.048 km centered over the airport (Fig. 1). This variation on the definition of the TAS accounts for curved approaches or departures and affords each airport the same treatment regardless of the number/orientation of runways. The radar coverage in each TAS is computed by projecting the radar beams onto 180 vertical transects, each centered over the airport and 1° apart (Fig. 1). The transects extend from the surface to 3.048 km and have a horizontal and vertical spacing of 250 and 10 m, respectively. The median beam height h along each transect is computed according to

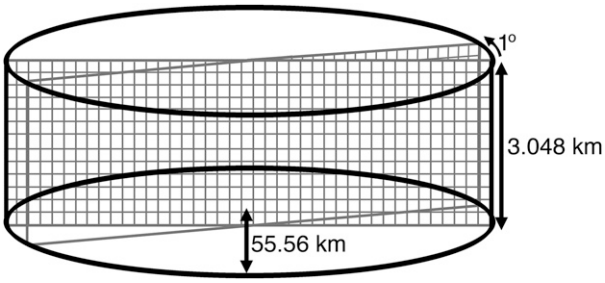

FIG. 1. Graphical depiction of a TAS (black cylinder) and the vertical transects (gray) used to compute the radar coverage.

$$h = R_s \sin(\phi) + \frac{R_s^2}{2 I_R R_e}, \tag{1}$$

where R_s is the slant range, ϕ is the tilt angle, I_R is the index of refraction (=1.21), and R_e is the radius of Earth. The beamwidth is given by $R_s\theta$, where the angular beamwidth θ is assumed to be 0.96°. This is the same as that used by the WSR-88D Radar Product Generator (C. Stephenson, Radar Operations Center, 2018, personal communication).

The radar coverage is computed for the five different volume coverage pattern (VCP) modes that are available in build 18 of the WSR-88Ds implemented in early 2018. These are VCPs 215, 12, 35, 121, and 31, which have the elevation angles, scan times, and recommended usage provided in Table 1. Note that we do not include VCP 32 as a separate mode as it has the same coverage pattern as VCP 31. Repeat scans of the low-elevation tilts, which is possible with select VCP modes, are also not relevant to this study and are not considered further.

3. Assessment of radar coverage in TASs across the CONUS

a. Overshooting and cone-of-silence effects

There are three controls on radar coverage/quality in a TAS. These are the airport-to-radar distance (A2R), the VCP mode, and terrain effects (defined in section 3b). The first two are evaluated in this section. Consider ERI (Erie, Pennsylvania) and BUF (Buffalo, New York).

TABLE 1. Attributes of the VCP modes discussed herein (from Radar Operations Center 2015). VCP modes retired as of January 2018 are indicated with an asterisk.

VCP	Scan time (min)	No. of tilts	Elevation angles (°)	Recommended usage
215	6	15	0.5, 0.9, 1.3, 1.8, 2.4, 3.1, 4, 5.1, 6.4, 8, 10, 12, 14, 16.7, 19.5	General-purpose precipitation, including tropical systems capable of producing tornadoes
12	4.15	14	0.5, 0.9, 1.3, 1.8, 2.4, 3.1, 4, 5.1, 6.4, 8, 10, 12.5, 15.6, 19.5	Severe weather, including tornadoes
35	7	9	0.5, 0.9, 1.3, 1.8, 2.4, 3.1, 4, 5.1, 6.4	Scattered to widespread light to moderate stratiform precipitation
121	6	9	0.5, 1.5, 2.4, 3.4, 4.3, 6, 9.9, 14.6, 19.5	Large number of rotating storms or tropical systems or when better velocity data are needed
31/32	9.75	5	0.5, 1.5, 2.4, 3.4, 4.3	Clear air, light rain, and/or wintry precipitation
11*	5	14	0.5, 1.5, 2.4, 3.4, 4.3, 5.3, 6.2 7.5, 8.7, 10, 14 16.7, 19.5	Convection, especially close to radar
21*	6	9	0.5, 1.5, 2.4, 3.4, 4.3, 6, 9.9, 14.6, 19.5	Shallow precipitation with embedded convection

The nearest radar to each of these airports is KBUF (Buffalo, New York; Figs. 2a,d) and both have negligible terrain effects. Vertical cross sections of beamwidth for VCP 12 are taken along the radar radial that transects the center point of each airport in order to show the full range of beamwidth and h across each TAS. There is a clear dependence on A2R in these cross sections, with ERI having much less of the TAS covered than BUF (Figs. 2b,e). The relative dependence on VCP mode is also evident. At ERI, the coverage is the same for both VCP modes (Figs. 2b,c). This is because only tilts below 1.5° sample this TAS and all VCP modes have coverage below this level (Table 1). At BUF, the different sizes of the cones of silence (CoSs) for VCPs 12 and 31 affect the total coverage—only about 5% of the top of the TAS is unsampled for VCP 12, while nearly 70% of it is unsampled for VCP 31 (Figs. 2e,f).

The amount of coverage in a given TAS may not be as important as whether the intended flight paths are covered. Typically, pilots aim for 1000 ft (304.8 m) of altitudinal change for every 3 n mi (5.556 km) of horizontal travel (the 3:1 rule), indicated in Fig. 2 as the red approach–departure slopes. At ERI, flights entering the TAS from the southwest have no radar coverage from KBUF along their flight paths. At BUF, the flight path is completely sampled regardless of the VCP mode, but this is only because the CoS is very close to BUF's center. If the radar is offset from the airport center some of the flight path will be unsampled, as is the case at MSP (Minneapolis, Minnesota), whose nearest radar, KMPX, is 27 km away (Fig. 2g). While most of the 3:1 line is sampled in VCP 12, a large fraction of it is unsampled in VCP 31 (Figs. 2h,i).

One can gain a more universal appreciation of how A2R and VCP mode impact the coverage in a TAS through consideration of a set of theoretical airport–radar pairings with no terrain effects. The percent of the TAS and flight path (given by the 3:1 line) sampled by the radar is provided in Figs. 3a and 3b. Regardless of the A2R or VCP mode, *there is no situation when all of the TAS is sampled* (Fig. 3a). When A2R is greater than about 80 km, overshooting—where the radar beam is above part or all of the TAS—leads to rapidly decreasing coverage with increasing A2R. There is also no dependence on VCP mode at these distances for reasons previously discussed. When A2R is less than about 80 km, overshooting and the CoS both affect coverage. The increasing loss of coverage from the CoS is counterbalanced by decreased overshooting as A2R is decreased indicating that the relative contribution from each is dependent on A2R. There is a local minimum in the flight-path coverage at an A2R of about 25 km for VCPs 35, 121, and 31 (Fig. 3b). This is due to the radar offset noted in Figs. 2g–i.

According to Figs. 3a and 3b, VCP-mode effects are apparent for smaller A2R, wherein VCP 31 has the least, and VCPs 215 and 12 have the most, coverage. The maximum difference in coverage is 14%; 55% of the airports are within 80 km of the nearest WSR-88D, making it useful to know if there is a preferred VCP mode during icing events. Identifying icing events at all 398 airports is rather difficult. Pilot reports (PIREPS) are customarily used for this exercise (e.g., Tafferner et al. 2003; Ellrod and Bailey 2007; Smith et al. 2012), but in this study, PIREPS are not useful because they are dependent on the number and type of aircraft—less busy airports may have icing conditions at some level in the TAS, but not have any aircraft there to sample it (Brown et al. 1997). Not all airports have remote sensing capabilities to allow for icing detection above the ground,

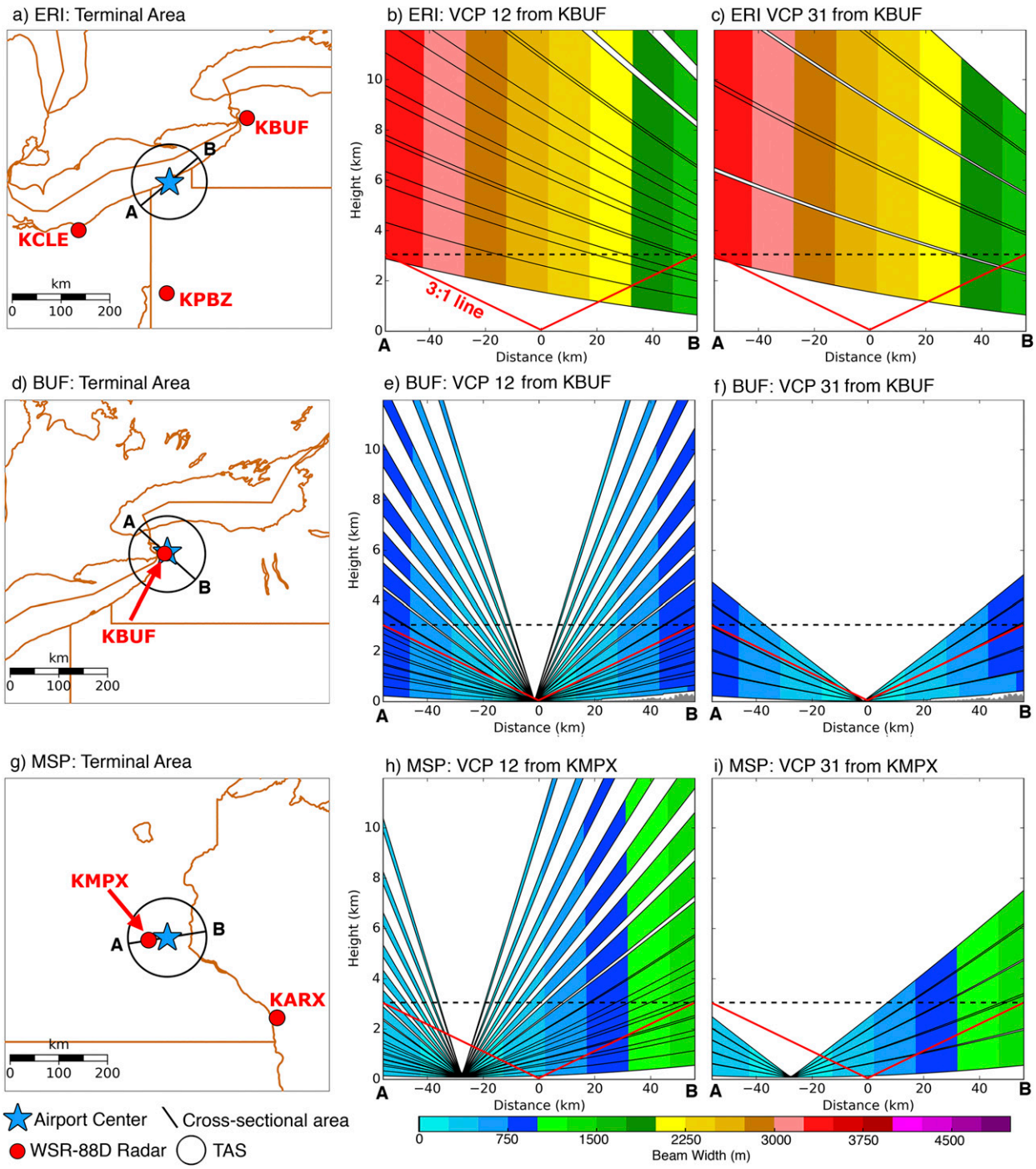

FIG. 2. (a),(d),(g) Maps showing TASs and nearby radars and vertical cross sections of beamwidth for (b),(e),(h) VCP 12, and (c),(f),(i) VCP 31 at (top) ERI, (middle) BUF, and (bottom) MSP. In the cross sections, the top of the TAS is given by the dashed line. The red line labeled 3:1 is the typical ascent–descent path used for aircraft flying into and out of the TAS. In these cross sections and all others, the indicated height is AGL.

either. The only observations *all* 398 airports share are those that come from the Automated Surface Observing System (ASOS) network. This network does not allow for all icing situations to be diagnosed, particularly when icing only exists aloft and no precipitation reaches the ground, and thus some incidents of icing in TASs will not be accounted for in this assessment. However, these types of icing conditions are generally dominated by cloud-sized particles, which cannot be detected by the WSR-88Ds (Bernstein et al. 1997) and, therefore, are

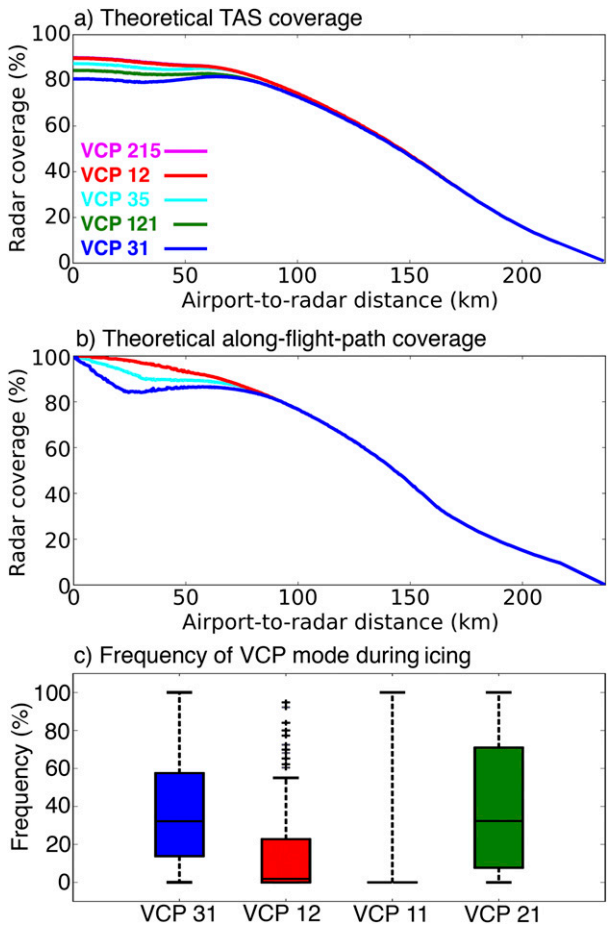

FIG. 3. The theoretical (i.e., assuming no terrain effects) (a) total TAS coverage, (b) along-flight-path coverage for all VCP modes, and (c) the frequency of VCP modes used during favorable icing incidents. Note that VCPs 215 and 12 have identical coverage in (a) and (b) and VCPs 121 and 31 have identical coverage in (b).

not the types of icing events where radars will be useful.

For this study, the 5-min ASOS observations are used to assess probable icing conditions. When FZRA, FZDZ, or ice pellets (PL) are observed, supercooled liquid water (SLW) is assumed to exist somewhere in the TAS (Hanesiak and Stewart 1995; Politovich and Bernstein 1995). However, ASOS are incapable of detecting FZDZ and PL—these are only recorded when a human observer augments the report (NOAA 1998). Therefore, in order to have a more comprehensive event climatology for airports/events without augmentation, icing conditions are also assumed to exist when the surface temperature is between 267 and 273 K *and* some form of precipitation or mist is reported. The inclusion of mist allows for errant misclassifications of FZDZ (Landolt et al. 2017). Though the above range of temperatures is conducive to the formation of SLW (e.g., Meyers et al. 1992; Petters and Wright 2015; Reeves et al. 2016), these conditions do not guarantee its presence. Because of this, we refer to all events as simply "favorable icing incidents" to distinguish them from confirmed icing events. The assessment is performed for winter months (October–March) starting in October 2013 and ending in March 2017.

Records of VCP modes from all WSR-88Ds during favorable icing incidents are assessed. The closest volume scan in time that precedes the observation is used. Multiple observations from the same volume scan are discarded. This yields 841 592 unique observation–volume scan pairs. During the evaluation period, VCPs 35 and 215 were not available and VCPs 11 and 21 (Table 1) were retired with build 18. The TAS coverage for VCP 11 is indistinguishable from VCP 12 (not shown). VCPs 21 and 121 have identical coverage patterns—they differ only in the number of times each tilt is sampled. VCP 121 performs multiple scans of the low-elevation tilts with varying pulse repetition frequencies and, hence, exerts considerable wear and tear on the radar's hardware.

Frequency of VCP use during favorable icing incidents is summarized in Fig. 3c. VCPs 31 and 21 are the most common modes during icing, with a slight preference toward VCP 21, a finding that merits some explanation. We can only speculate on the motive for using this VCP during these events, but a likely reason is that it provided a good compromise: It allowed for higher tilts to be sampled without taxing the hardware unnecessarily. Now that VCP 21 has been retired, it is unclear what mode will take its place. VCP 35 is the most similar in the number of tilts and scan time (Table 1). It also affords slightly more coverage in the TAS and along flight paths (Figs. 3a,b). However, this VCP mode lacks coverage above 6.4°, which may affect whether key microphysical signatures are detected (section 4).

Any VCP mode that terminates at an elevation angle greater than 5° may invoke the Automated Volume Scan Evaluation and Termination (AVSET) option in which the scan is terminated at tilts 6° or higher if the reflectivity does not meet certain criteria (Chrisman 2009). However, AVSET was only used 3% of the time when the radars were in appropriate modes and, hence, is not a significant limiter of TAS coverage during favorable icing incidents.

b. *Terrain effects*

Reduced radar coverage in the TAS also occurs when terrain blocks one or more of the radar tilts or when the airport is at a lower altitude than its nearest radar. For example, SGU's (Saint George, Utah) nearest radar, KICX (Cedar City, Utah), is only 86 km away (Fig. 4a), but it is 2335 m *higher* than the airport. This leads to consequential overshooting (Fig. 4b) and a 72%

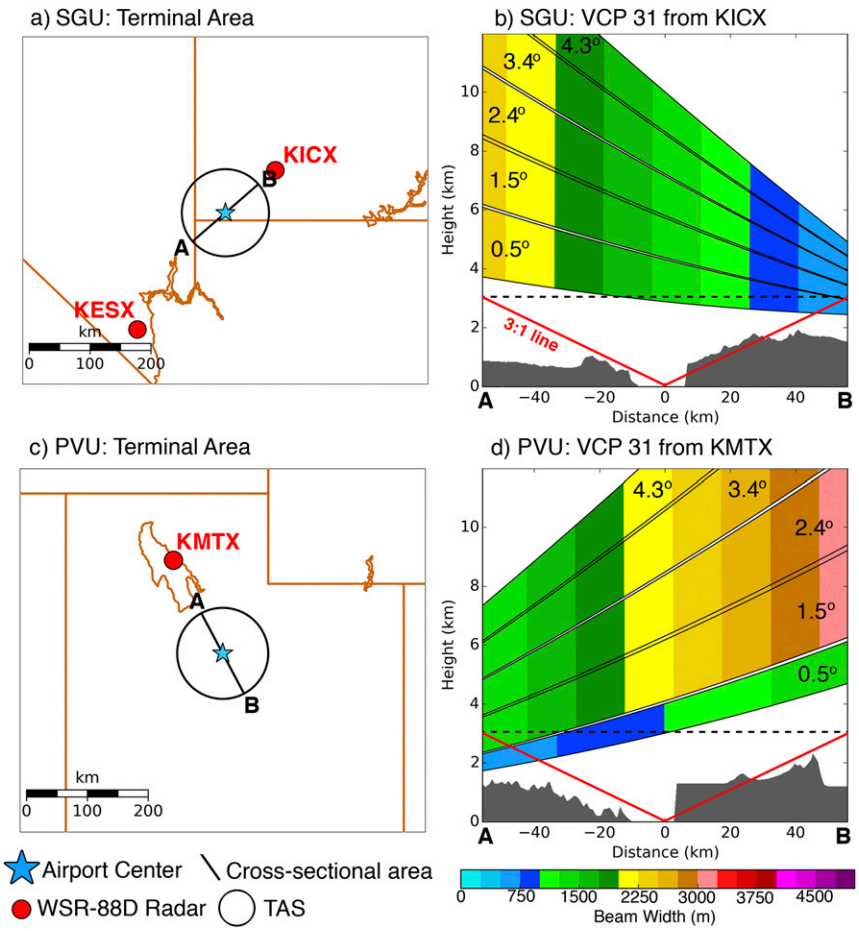

FIG. 4. As in Fig. 2, but showing only VCP 31 and for (a),(b) SGU and (c),(d) PVU. The gray shading in (b) and (d) represents the terrain.

(76%) decrease in the total TAS (flight path) coverage relative to when there are no terrain effects. Another example is PVU (Provo, Utah; Figs. 4c,d). In this case, the airport and radar are at comparable altitudes, but there is significant blockage of the 0.5° tilt leading to a drop in the total TAS (flight path) coverage of 44% (48%) relative to when there are no terrain effects.

The *actual* coverage, accounting for terrain effects, for VCP 31 is computed using the Shuttle Radar Topography Mission (SRTM) terrain-elevation data with a 1-arc-s (~30 m) resolution.[1] About 90% of the airports suffer from some degree of terrain effects, but for most of these (64%), the coverage is within 5% of the theoretical values from section 3a (Fig. 5a). The combined effects of terrain, the CoS, and overshooting across the entire airport network yields 40 airports that have less than 25% of their TASs covered (Fig. 5b). These are mostly in the western United States and northern plains, but airports in the Appalachian Mountains also have somewhat reduced coverage.

c. *Radar coverage by traffic and vulnerability to icing*

The actual TAS coverage is sorted by the number of annual enplanements in 2016 (Fig. 5c). Of the 29 large-hub airports (>8 million enplanements), 18 of them have TAS coverage ranging from 80% to 90%. The amount of coverage for lower-trafficked airports is hit or miss, with some having very good coverage and others no coverage at all. For reference, the spatial distribution of airports by traffic is shown in Fig. 5d. There are several medium- and large-hub airports along the west coast that have limited

[1] In the following analyses, beams that are more than 50% blocked are discarded. This decision is based on the power-return function for the WSR-88Ds [Eq. (3)], which ranges from 1 at the center of the beam to near 0.4 at an angular distance of 0.5° (Doviak and Zrnić 1993). Such a distribution indicates that beams that are more than half blocked may have too low an SNR for meaningful interpretation. However, we note there are no published FAA standards on this topic.

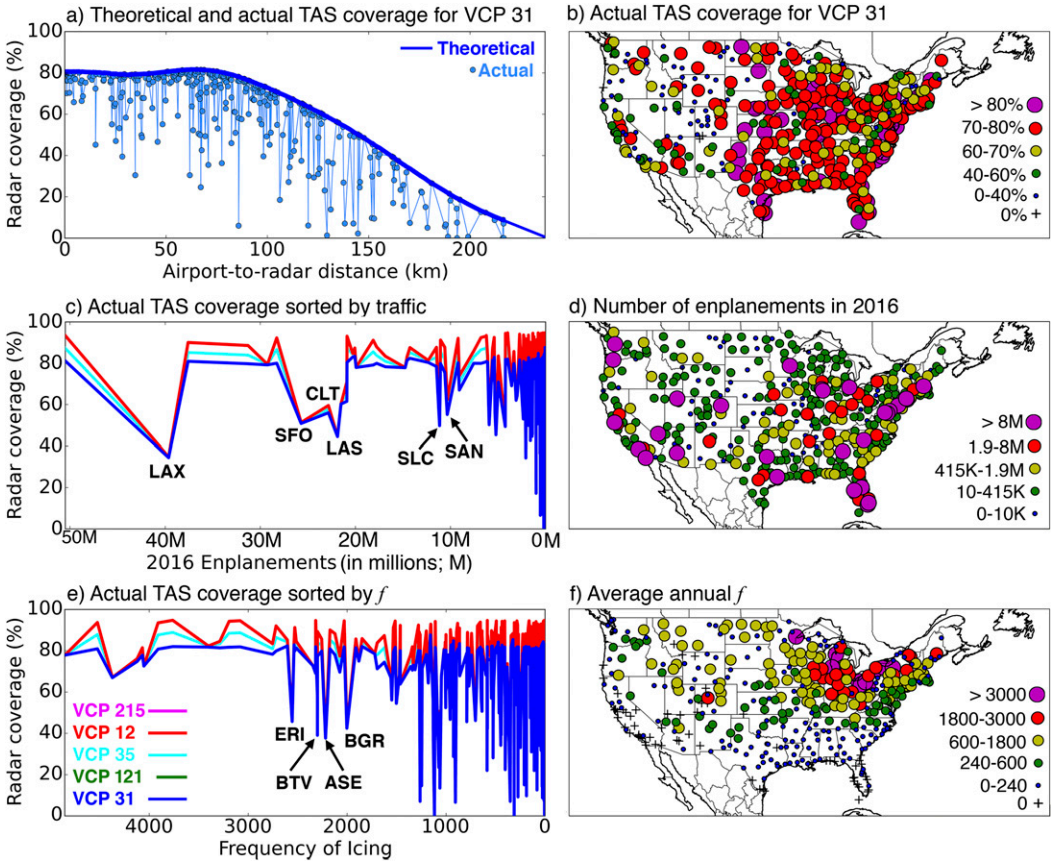

FIG. 5. (a) Theoretical and actual TAS coverage sorted by A2R. Actual TAS coverage sorted by (c) the number of annual enplanements and (e) the frequency of icing f. Spatial distributions of the (b) TAS coverage, (d) number of enplanements, and (f) average annual f.

TAS coverage because of terrain effects, such as LAX (Los Angeles, California; cf. Figs. 5b,d).

The TAS coverage as a function of the average yearly number of favorable icing incidents f (determined as in section 3a) is shown in Fig. 5e. The higher-f airports do tend to have more radar coverage (between 70% and 90%), but there are some exceptions as indicated. A map of f by airport shows icing is most common around the Great Lakes and upper Midwest (Fig. 5f). But, several airports across the northern United States and intermountain west have enhanced f. Some of these have very poor radar coverage, particularly those in the vicinity of Salt Lake City, Utah, and near the border between Montana and North Dakota (cf. Figs. 5b,f).

d. *Effect of anomalous propagation*

Thus far, we have assumed an I_R of 1.21 in calculations of h, which is the same as that used by the WSR-88D Radar Product Generator and is representative of a standard atmospheric lapse rate. In reality, I_R varies with density. In most situations, the difference in h is small compared to the beamwidth so errors in h have little effect on interpretation. But when temperature inversions exist, the errors in h can be significant because of anomalous propagation or superrefraction of the radar beam (Doviak and Zrnić 1993).

To assess the probable frequency of superrefraction, ASOS observations taken coincident in time and space with radiosonde launches are queried for their favorable icing conditions for the winter seasons from 2006/07 to 2016/17. This longer time window is used to increase the number of soundings, since the temporal and spatial resolution of soundings is comparatively low. There are 2637 soundings associated with the favorable icing incidents; 79% of these have an inversion below 3.048 km, consistent with findings from other investigators (Bernstein et al. 2018, manuscript submitted to *J. Appl. Meteor. Climatol.*). The inversions vary in height AGL and intensity widely enough that no single I_R adequately characterizes these types of events. But an extreme example from a strong

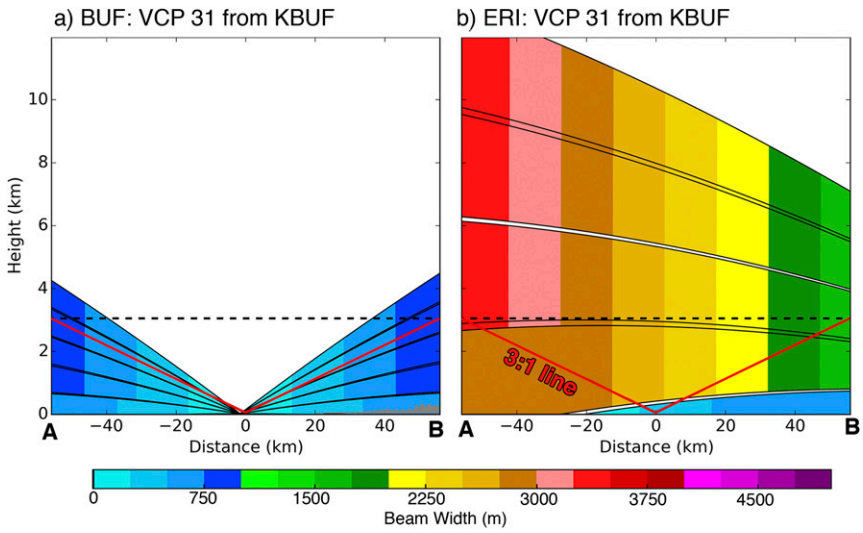

FIG. 6. As in Fig. 2, but using a temperature profile with a strong inversion. Locations of the cross-sectional areas (AB) are indicated in Figs. 2a and 2d.

surface-based inversion is applied to ERI and BUF for VCP 31. At both airports the 0.5° tilt intersects the ground, but all tilts are considerably lower than when a standard I_R is used (cf. Figs. 2c,f and 6a,b). For this example, when A2R is greater than 136 km, the error in beam height exceeds the depth of the TAS. While this is an extreme example, it underscores the fact that during icing events, h is very likely overestimated. Unfortunately, computing the I_R along each radar beam is not practical given current observational and computing constraints. Therefore, attempting to diagnose the tops and bottoms of icing layers using only radar data in order to diagnose icing along flight paths is a potential safety hazard.

Anomalous propagation is not only problematic for its effects on h, it also leads to increased ground clutter, which can overwhelm the echo produced by precipitation. An example of this is shown at BUF at 1030 UTC 18 December 2016 using the mosaicked base reflectivity from the Multi-Radar/Multi-Sensor (MRMS; Smith et al. 2016; Zhang et al. 2016) system. This is in the middle of a light FZRA event, according to ASOS reports at BUF. Before quality control (Tang et al. 2014) is imposed, there is weak to moderate echo throughout the TAS (Fig. 7a). A considerable amount of this echo is removed during quality control because of the rather low correlation coefficient in this area (Figs. 7b,c). The fraction of pixels flagged as nonmeteorological by the MRMS system are consistent with those categorized as ground clutter by the level 3 Hydrometeor Classification Algorithm (L3HCA; Park et al. 2009) product (not shown).

To gain a more comprehensive appreciation of the effects of ground clutter during favorable icing incidents,

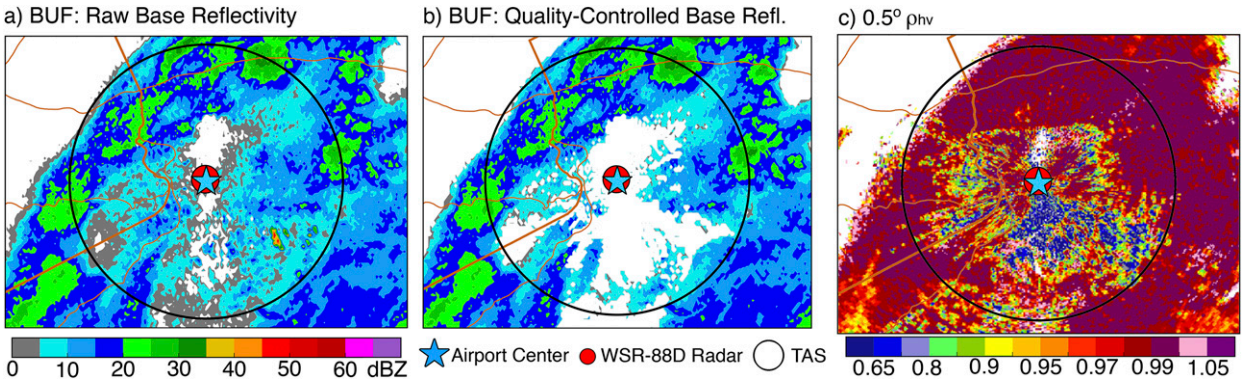

FIG. 7. The (a) raw and (b) quality-controlled MRMS base reflectivity mosaic and (c) the 0.5° correlation coefficient from KBUF at 1030 UTC 18 Dec 2016.

TABLE 2. The frequency of favorable icing events *f* along with the mean percentage and standard deviation of pixels from the L3HCA that are identified as nonmeteorological.

Airport	*f*	Mean (%)	St dev (%)
YNG (Youngstown, OH)	4852	20.26	25.39
BUF (Buffalo, NY)	4523	87.75	17.73
SYR (Syracuse, NY)	4373	25.27	27.65
TVC (Traverse City, MI)	4122	56.21	29.81
CAK (Canton/Akron, OH)	4069	22.19	22.89
ROC (Rochester, NY)	4052	17.14	21.54
CLE (Cleveland, OH)	3910	23.76	18.33
PIT (Pittsburgh, PA)	3763	22.00	16.60
LAN (Lansing, MI)	3402	16.26	27.53
MKG (Muskegon, MI)	3287	14.38	20.19

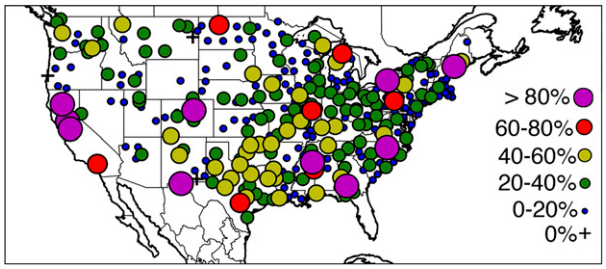

FIG. 8. The percentages of echo flagged as nonmeteorological for all favorable icing incidents.

the L3HCA output for the cases used in Fig. 3c is queried and the percentage of pixels from the 0.5°-elevation tilt that are flagged as nonmeteorological relative to the total echo is computed for all TASs. Table 2 lists the mean percentages of clutter over all events and for the highest-*f* airports and shows that not all airports are equally affected—BUF has a rather high mean while MKG (Muskegon, Michigan) is comparatively low. The mean percentages across all airports are provided in Fig. 8. Only 17 airports have means that exceed 60%. The airports most compromised are those with small A2R and/or nearby low-lying terrain. However, though a low mean may suggest that clutter contamination is not a pathological problem, it does not suggest it is a *nonexistent* problem. Consider the standard deviations in Table 2. These are all quite high (>16%), indicating that clutter can be a significant problem even at airports that usually are not that affected, thus underscoring the potential danger in relying solely on radar-detected icing for terminal airspace traffic management.

4. Beamwidth and VCP-mode effects on interpretation of radar returns

Coverage is but one piece of the puzzle. The radar's wavelength and beamwidth dictate whether icing can even be resolved. Many instances of icing cannot be captured by the WSR-88Ds, such as events dominated by cloud-sized particles (Bernstein et al. 1997, 2018, manuscript submitted to *J. Appl. Meteor. Climatol.*). Even if the particles are precipitation sized, the SLW has to be within the radar volume. So, even though there has been some research suggesting that near-ground refreezing can be detected by the WSR-88Ds in certain situations (Kumjian et al. 2013), overshooting frequently leaves these layers unsampled. Therefore, we focus on the production of SLW aloft and within precipitating clouds. There are some dual-polarized signatures that indicate the presence of SLW, but these signatures can be ambiguous and lead to false positives (Hudak et al. 2002; Wolde et al. 2003; Field et al. 2004; Plummer et al. 2010). We instead consider two signatures—dendrite growth and melting—that usually, though not always, indicate icing is not favored. Unless the atmosphere is saturated with respect to both ice and liquid water, dendrite production is not favorable for icing as this hydrometeor type grows quickly and tends to rapidly scavenge SLW. As the dendrites fall out of the growth zone, they sweep out supercooled liquid water droplets in their paths. Melting is also not favorable for icing for obvious reasons. Therefore, the presence of these layers can be used to infer that icing is not a likely threat in the intervening layer. But when they do not exist, this could be a strong indicator icing conditions do exist, at least in stratiform precipitation systems.

An example of dual-polarized returns for an environment with both a dendrite growth zone (DGZ) and a melting layer (ML) is provided for a FZRA event at KDDC (Dodge City, Kansas). Figures 9a–c show quasi-vertical profiles (QVPs; Ryzhkov et al. 2016) for the 10° tilt from the volume scan initiated at 1406 UTC 15 January 2017.[2] The DGZ and ML are indicated in each panel. [The reader is referred to Kumjian (2013a,b) for more information on extracting microphysical processes from dual-polarized radar observations.] Assuming these profiles are horizontally uniform, time invariant, and that they start at 0 km AGL, then any transect through any airport should appear as in Figs. 9d–f. In this transect, the ML is within the TAS while the DGZ is above it.

These transects are sampled as though with KBUF at BUF and ERI following the methodology in

[2] The reader may note that the profiles in these figures do not extend to the surface but rather terminate about 300 m AGL. This is because the first eight gates are discarded by the WSR-88Ds because of sidelobe contamination.

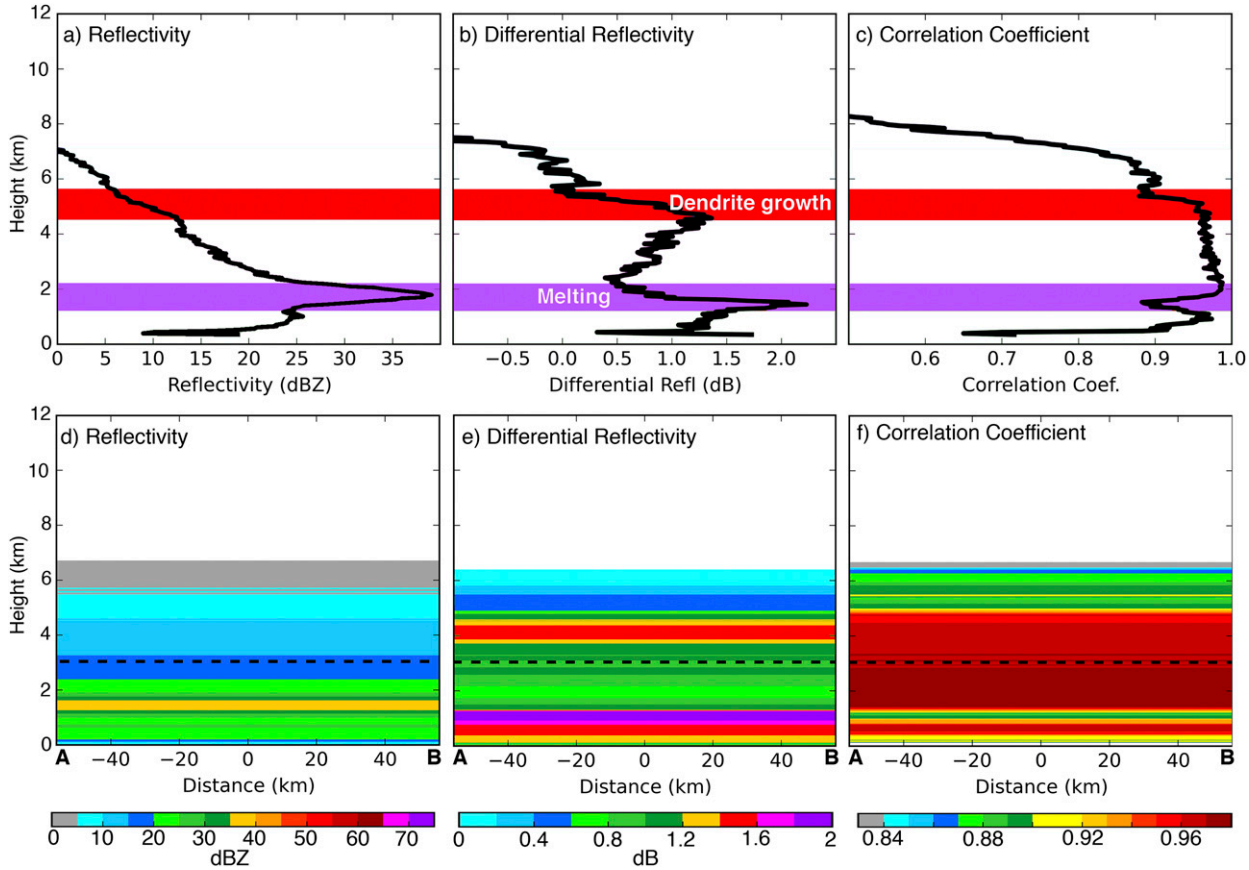

FIG. 9. QVPs of (a) reflectivity, (b) differential reflectivity, and (c) correlation coefficient at 1403 UTC 15 Jan 2017 from KDDC. Microphysical processes as inferred from the radar moments are indicated. (d)–(f) Vertical cross sections through an airport transect for the QVPs shown in (a)–(c), respectively. In (d)–(f), the top of the TAS is indicated by the dashed line.

Ryzhkov (2007). Namely, the assumed return at any point along a beam is given by

$$M = \frac{\sum_i M_i P_{Ri}}{\sum_i P_{Ri}}, \tag{2}$$

where M is the radar moment (i.e., reflectivity Z_H, differential reflectivity Z_{DR}, cross-polar correlation coefficient ρ_{hv}) and P_R is the power return at that point in the beam. The value of P_R used here is that which has been empirically determined as representative of the WSR-88Ds:

$$P_R = 5.405\left|\frac{4!1.68J_4\left(\frac{D_d \sin\alpha}{\lambda}\right)}{\frac{D_d \sin\alpha}{\lambda}} + \frac{0.16J\left(\frac{D_d \sin\alpha}{\lambda}\right)}{\frac{D_d \sin\alpha}{\lambda}}\right| \tag{3}$$

(Doviak and Zrnić 1993). In Eq. (3), J_4 and J are fourth- and first-order Bessel functions, D_d is the diameter of the reflector, α is the angular distance from the beam axis, and λ is the radar wavelength. Examples of how these moments appear at BUF for VCP 31 are provided in Figs. 10a–c. The ML is clearly evident in all three moments. There is also a subtle signature of the DGZ in the highest tilt of Z_{DR}, but it is not obvious this is a DGZ given that most of this layer is in the CoS. A broader view showing the moments at a greater horizontal range from the radar would allow the user to determine that there is DGZ present (not shown), but broadening the area only works when the stratification is horizontally uniform. Strong gradients in the dual-polarized moments along frontal zones, or spotty coverage from isolated cells may make the diagnosis of a DGZ over the TAS impossible for this VCP mode. VCP 12, because it has overlapping tilts below 5°, shows a better-defined ML (Figs. 10d–f). Its higher-elevation tilts also allow for more reliable detection of the DGZ.

The same exercise is repeated for ERI and highlights the dangers of relying on these signatures to infer whether icing may exist for airports with larger A2Rs. For VCP 31, the ML is contained within the radar volume toward the northeast end of the transect, but it is not resolved (Figs. 10g,h). The DGZ is within the radar

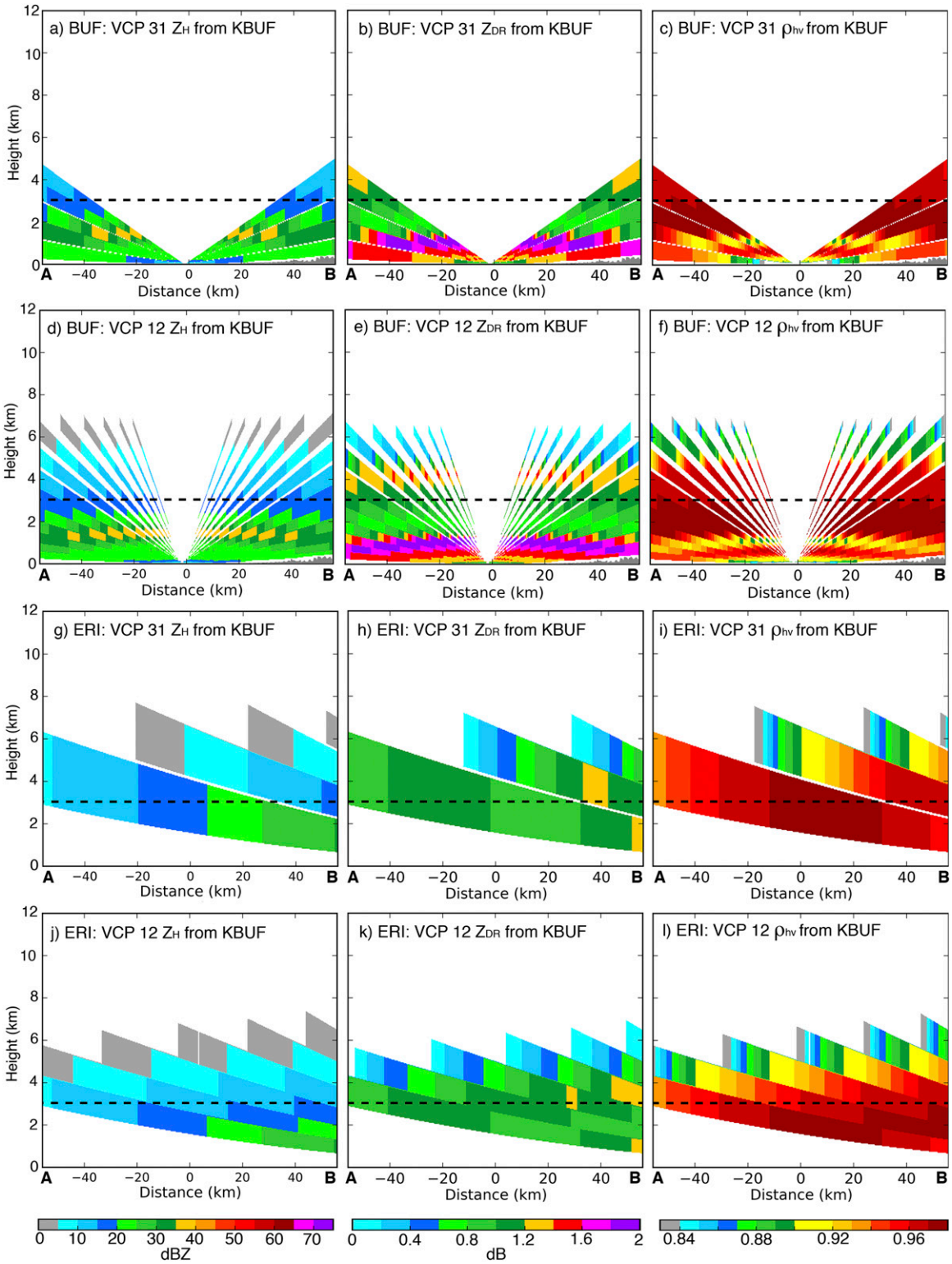

FIG. 10. Vertical cross sections of (left) Z_H, (center) Z_{DR}, and (right) ρ_{hv} at (a)–(f) BUF and (g)–(l) ERI when sampled with (a)–(c),(g)–(i) VCP 31 and (d)–(f),(j)–(l) VCP 12. The cross-sectional areas are indicated in Figs. 2a and 2d. The top of the TAS is indicated by the dashed line.

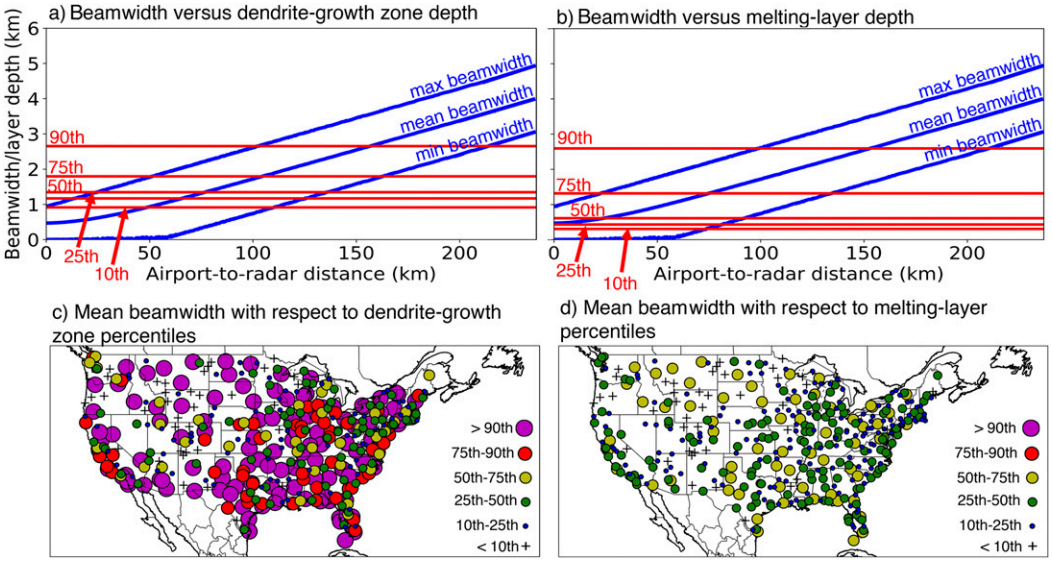

FIG. 11. (a),(b) The maximum, mean, and minimum beamwidths (blue) as a function of A2R and select percentiles from the range of microphysical layer depths (red) and (c),(d) the mean beamwidth relative to the dendrite-growth and melting-layer-depth percentiles.

volume over the entire TAS, but the beams are broader than the depth of this layer and, hence, it is not resolved either. The situation is only slightly improved for VCP 12 in that the DGZ is marginally detected for Z_{DR} (Figs. 10j–l). Therefore, an apparent lack of a DGZ or ML are not good indicators that icing is present. In reality, those layers exist—they just cannot be resolved at this airport.

Using radar observations to determine typical DGZ and ML depths is not feasible given noise, calibration issues, and canting angle effects (Ryzhkov et al. 2002, 2005a; Bechini et al. 2008), but the depths of these layers can be inferred from radiosondes. Any layer in a sounding taken coincident with some form of precipitation that is both saturated and has a wet-bulb temperature ranging from 255 to 263 K is defined as a DGZ (e.g., Bailey and Hallett 2009). Any layer that has temperature ranging from 273 to 275 K is defined as a ML (Auer 1974; Yang et al. 1997; Rohrer 1989; Motoyama 1990; Dai 2008; Kienzle 2008). This assessment is performed at all radiosonde sites in the CONUS for the 2006/07–2016/17 winter seasons.

There are 20 376 (12 348) soundings with a DGZ (ML). The medians, quartiles, and deciles for these layers are considered with respect to the range of beamwidths across a TAS as a function of A2R (Figs. 11a,b). There are three possible regimes in either figure:

1) When the maximum beamwidth is less than the median layer depth, then the typical layer can be resolved throughout the TAS. For the DGZ analysis, 63 airports meet this criterion (Fig. 11a). No airports meet this criterion for the ML (Fig. 11b).
2) When the minimum beamwidth exceeds the median layer depth, then the typical layer cannot be resolved anywhere in the TAS. There are 61 and 150 airports in this regime for the DGZ and ML, respectively.
3) When the median layer depth is between the maximum and minimum beamwidths, the typical layer can be resolved over at least part, but not all of the TAS. There are 274 and 248 airports in this regime for the DGZ and ML, respectively.

The spatial distribution of mean beamwidth with respect to the layer-depth percentiles is provided in Figs. 11c and 11d. In this analysis, an airport that is in the 90th percentile resolves the layer 90% of the time; 119 airports reach this threshold for the DGZ. These are airports whose nearest radar is within the TAS. But, most airports (191) are in the 10th–25th percentiles. No airports meet the 90th percentile for the ML. The above percentages should not be taken as literal rates for the frequencies at which these layers are resolved, but rather as best case scenarios, as they assume the layers are within the radar volume. The closer the ML is to the ground, the more likely the radar will overshoot it. Higher-altitude DGZs are more likely to be contained in the CoS, making them more difficult to identify.

5. A multiradar approach

Until now, only coverage from the closest radar has been considered. Whether other radars that sample the TAS are able to fill coverage voids is determined by

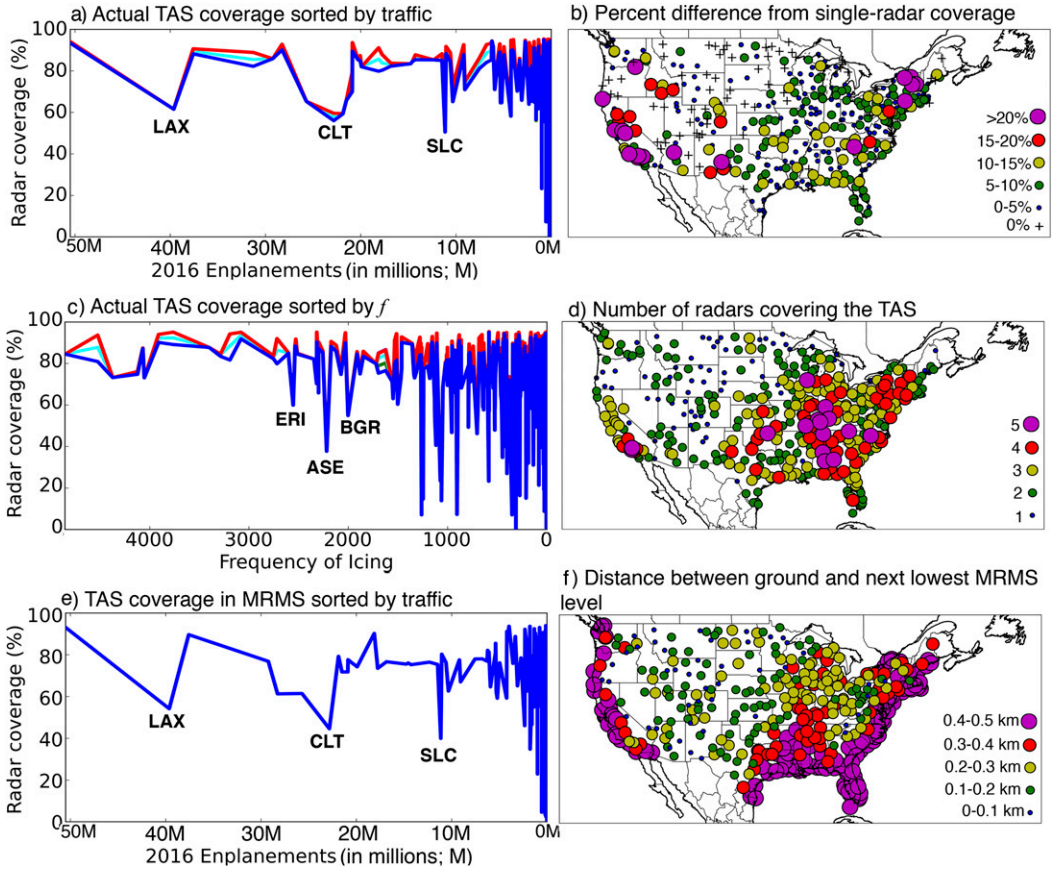

FIG. 12. (a),(c) As in Figs. 5c and 5e, respectively, but accounting for the coverage from all radars that sample the TAS, (b) the percentage difference in TAS coverage obtained when using all radars relative to only the nearest one, (d) the number of radars with coverage in each TAS (not accounting for terrain effects), (e) the TAS coverage in the MRMS mosaic, and (f) the distance between the altitude of the airport and the next highest MRMS level. The line colors in (a) and (b) are as in Figs. 3a and 3b.

computing the total TAS coverage accounting for *all* radars that sample it. Though the dependence on VCP mode is reduced, this analysis shows only modest increases in coverage relative to when only the nearest radar is used (cf. Figs. 5c,e and 12a,c). Airports with less than 60% coverage are indicated and are mostly the same as in Fig. 5. A map of the percentage difference in TAS coverage for a single versus multiradar approach shows there are a few isolated regions, such as along the California coast, where coverage is greatly enhanced, but for most airports, the increase ranges from 5% to 15% (Fig. 12b). The least benefitted are those airports in the northern plains, several of which have no increased coverage.

Figure 12d shows the number of radars having coverage at each airport. Several airports in the Mississippi valley, the northeastern United States, and Southern California have coverage from four or five radars. Interrogating several radars for several airports may be unreasonable given the timelines for which decisions need to be made in the aviation sector. This makes using a three-dimensional (3D) radar mosaic a potentially attractive option. The National Weather Service does generate a 3D mosaic using the MRMS system. MRMS has a vertical grid spacing ranging from 250 m to 1 km and a 1-km horizontal grid spacing. The coverage in each TAS from MRMS averaged over the month of December 2016 is very close to, but somewhat less than, what is computed when using all radars (cf. Figs. 12a and 12e). The primary cause for this is low-level gaps in coverage between the ground and the first MRMS level above it. These range from 0 to 0.5 km, with an average depth of 0.29 km (Fig. 12f). Over most of the CONUS, there is no radar coverage in the gap because of overshooting, but within 0–85 km of each radar (depending on the distance between the ground and nearest MRMS layer above it), near-surface returns are not being incorporated into the MRMS mosaics. The airports most

affected by the gap are those that are close to sea level where there is a nearly 0.5-km distance between the ground and lowest MRMS level. These are mostly along the coasts and in the southern Mississippi valley, but some airports in the Great Lakes area, where the vulnerability to icing is the highest, also have a larger gap.

A potential pitfall of using mosaicked reflectivity is the effect of interpolating from radar to Cartesian coordinates. It has been hypothesized that the vertical interpolation scheme in MRMS smears out vertical maxima in the radar moments (Lakshmanan et al. 2006). To investigate this, the vertical cross sections in Figs. 9d–f are sampled as though at ERI and MSP with all surrounding radars and interpolated to the coordinate system of the MRMS mosaics using the same vertical interpolation scheme as in MRMS (Lakshmanan et al. 2006). MSP is used over BUF for this exercise because only one radar samples that TAS. The vertical cross sections of single-radar coverage for BUF (Figs. 10a–f) are similar to those for MSP (not shown). A nearest-neighbor technique is used to mosaic these radars. This is different from the distance-weighted means used in the MRMS system (Lakshmanan et al. 2006), but is used here to make the boundaries between radars more distinct. Since Z_{DR} most clearly shows the DGZ and MLs, we restrict this analysis to only that moment.

ERI is one of the airports more benefitted by a multiradar approach as it has coverage from five nearby radars, leading to an increase in the total TAS coverage of 15% (Fig. 13a). When all surrounding radars are in VCP 31, ERI does not greatly benefit from a multiradar mosaic, as neither the ML nor the DGZ are apparent (Fig. 13c). When VCP 12 is used, there is evidence of a DGZ (Fig. 13e). One may also infer the presence of a ML that is partially overshot by the lowest beam. In this example, the degradation of signal relative to the truth is not due to vertical interpolation but rather to beam broadening (cf. Figs. 9e and 10h).

The only other radar with coverage for MSP (KARX; LaCrosse, Wisconsin; Fig. 2g) does not ameliorate the CoS issue (Fig. 13b), and including it only increases the TAS coverage by 2%. Hence, the primary difference between VCPs 31 and 12 is the CoS—otherwise both VCP modes resolve the DGZ and MLs (Figs. 13d,f). MRMS's vertical interpolation scheme does lead to a smaller Z_{DR} maximum in the DGZ relative to truth and even what is resolved by the radar (cf. Figs. 9e, 10e, and 13f). For DGZs that are less pronounced, this could be problematic. MSP reveals another important side effect of using a multiradar approach. That is that there can be jarring transitions in beamwidth where the observations from multiple radars abut. KARX has beamwidths on the order of 3 km adjacent to KMPX beamwidths on the order of 0.5–1 km (Fig. 13b). As a consequence, the DGZ seems to disappear in the CoS in both VCP modes. When the coverage is horizontally uniform, this type of artifact is easily identified. But in many winter storms, the coverage is not uniform as noted above. This lack of horizontal stratification or differences in VCP modes between radars that sample a given TAS will make identification of key microphysical signatures more difficult, regardless of whether one uses a single- or multiradar approach.

6. Conclusions and recommendations

This investigation has focused on the feasibility of using dual-polarized radars to infer the presence of icing in terminal airspaces (TASs) for all commercial airports in the CONUS. The first aim was to quantify the amount of coverage in each TAS as a function of its location, amount of traffic, and vulnerability to icing. The dependence on the distance between the airport and its nearest radar (A2R) is as expected: As A2R increases, overshooting increases, and the coverage decreases. When A2R is less than 80 km, VCP mode dictates the amount of coverage. Convective VCPs (i.e., those with higher elevation angles) provide slightly more coverage than those that terminate at lower angles, but no combination of VCP mode and A2R allows for all of the TAS to be sampled.

Terrain effects are another significant control on TAS coverage: 90% of the airports have some degree of terrain blockage and 40 airports could be described as severely impacted (i.e., having less than 25% of the TAS covered). As expected, airports most affected by terrain are in the Intermountain West and Appalachian Mountains.

It is not uniformly true that large-hub airports have good radar coverage. Six of them have less than 60% of their TASs covered. All large-hub and several medium-hub airports have a Terminal Doppler Weather Radar (TDWR) on site. This does raise an interesting question of the efficacy of the TDWR network for detecting icing conditions. An assessment of this is beyond the scope of this paper, especially given that there are several fundamental differences between these radars and the WSR-88Ds. These differences include single-polarization rather than dual-polarization, C band as opposed to S band, and different VCP configurations. An evaluation of the TDWR capabilities for detecting icing is recommended. It is also not uniformly true that airports with a high vulnerability to icing have good radar coverage. There are four airports that have a high frequency of favorable icing conditions f and several more with moderate f that have less than 60% of their

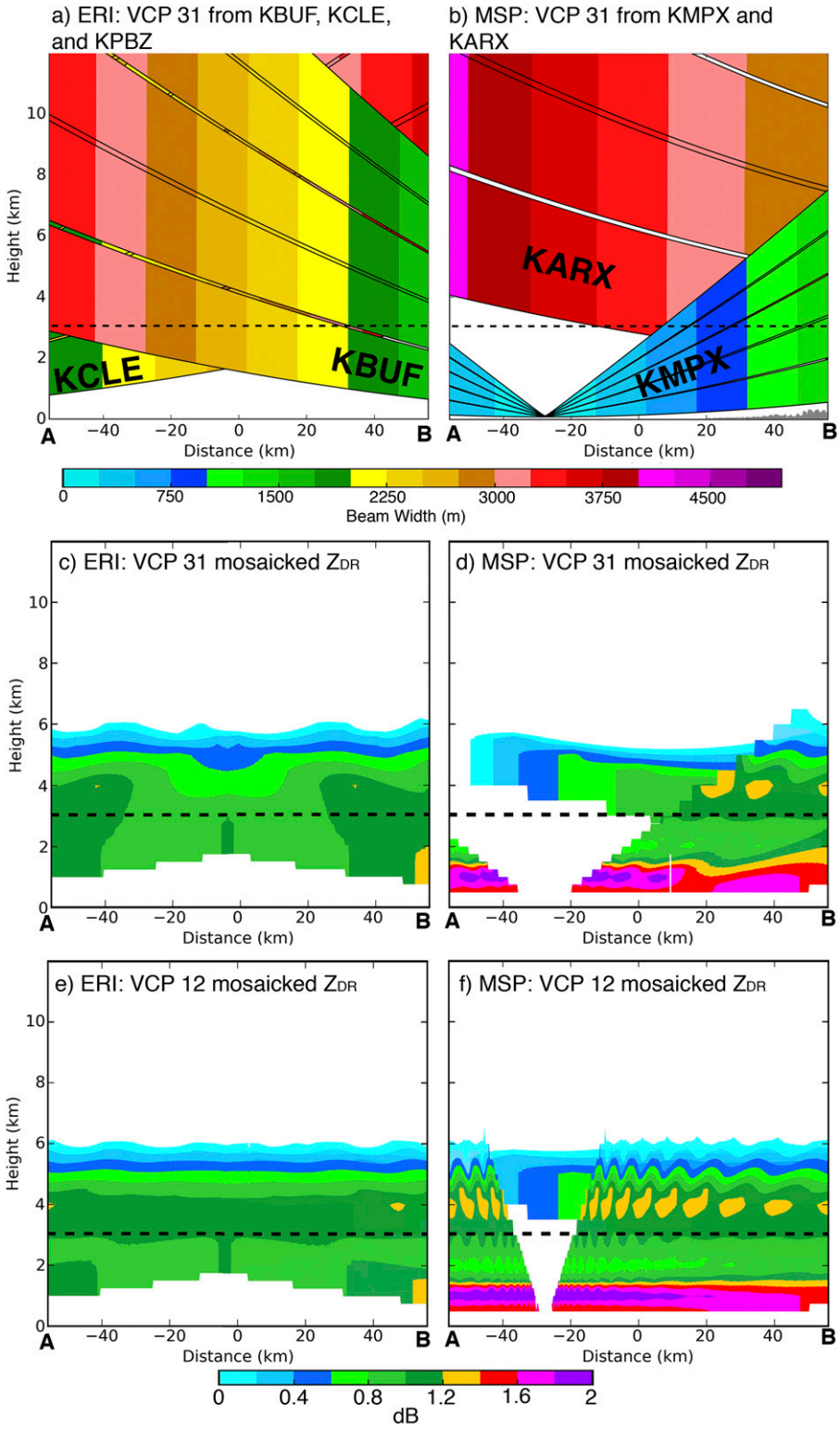

FIG. 13. (a),(b) As in Figs. 2c and 2i, but showing all radars with coverage in these TASs assuming VCP 31 and vertical cross sections of mosaicked Z_{DR} for (c),(d) VCPs 31 and (e),(f) VCPs 12 at (left) ERI and (right) MSP.

TAS covered. Consideration of additional ways of detecting icing is recommended for these sites.

Assessment of typical thermodynamic profiles during favorable icing conditions demonstrates that inversions of varying magnitude exist the majority of times, potentially leading to superrefraction, or even beam ducting, and significant echo contamination from ground clutter. Measurements of this across the airport network reveal that a large fraction of echo can be eliminated during quality control, especially at airports with a small A2R. It may be possible to use data-mining techniques to distinguish between clutter in the presence of icing and clutter in clear air (e.g., Ice et al. 2005), and thus use these thresholds to improve upon hydrometeor classification for icing, but this has yet to be conclusively demonstrated. Additional work in this area is recommended.

Superrefraction also has the negative side effect of leading to errors in the presumed h. In extreme cases, these errors exceed the depth of the TAS. Hence, the elevation of icing layers derived from radar observations will almost always be overestimated. This implies that icing layers may extend closer to the ground than indicated and suggests that attempting to diagnose icing tops and bottoms using only radar-derived products is a potential safety hazard. At the very best, one can use radar-derived icing tops to determine whether icing exists somewhere in the column below that point.

The effects of radar coverage on the diagnosis of microphysical processes reveals important limitations for those airports that have a radar in their TAS. When the radars are in VCP 31 or 35, some signatures, like the DGZ, may be left unsampled within the CoS over the airport. This would seem to indicate that convective VCPs are always preferable because of their smaller CoSs. But, a decision to favor convective VCPs during icing events needs to be balanced against the potential downfalls. Convective VCP modes are more wearing on the hardware. Additionally, using a long-pulse VCP (i.e., VCP 31) will result in a higher signal-to-noise ratio (SNR), the benefits of which have not been quantified herein. Previous investigators have found that this increased sensitivity is up to 10 dB for the WSR-88D network (D. Zrnić 2018; personal communication). Future research in this area is recommended. In cases where the radar is sufficiently far from the airport, some signatures, like the ML, may be overshot and beam broadening may cause it or other signatures to be unresolved. As stated above, other methods to determine whether icing exists in the TASs of airports with this issue are recommended.

A multiradar approach was considered wherein all radars with coverage in each TAS were evaluated. On average, this only increased the TAS coverage between 5% and 15%, and many of the same high-traffic or high-f airports that had reduced coverage with only one radar were only marginally aided through the inclusion of other radars. Using a multiradar approach requires the meteorologist to mentally stitch together multiple tilts from multiple radars to compile a complete picture of the TAS—a time-consuming exercise. Therefore, 3D mosaics were assessed. Using multiple radars did allow for some microphysical signatures to be better captured. However, issues with CoSs and beam broadening still manifest themselves in the mosaic. Perhaps one way to mitigate this issue is to provide the end user with a mosaic of beamwidth to allow them to more intelligently interpret the returns. Future efforts to this end are recommended.

Acknowledgments. Special thanks to B. Bernstein, S. Cocks, and J. Zhang. Funding was provided by NOAA/Office of Oceanic and Atmospheric Research under NOAA–University of Oklahoma Cooperative Agreement NA11OAR4320072, U.S. Department of Commerce and the National Research Council. This material is based upon work supported by the National Science Foundation under Grant AGS-1560419. Funding for H. Reeves was provided by the Federal Aviation Administration.

REFERENCES

Auer, A. H., 1974: The rain versus snow threshold temperatures. *Weatherwise*, **27**, 67, https://doi.org/10.1080/00431672.1974.9931684.

Bailey, M. P., and J. Hallett, 2009: A comprehensive habit diagram for atmospheric ice crystals: Confirmation from the laboratory, AIRS II, and other field studies. *J. Atmos. Sci.*, **66**, 2888–2899, https://doi.org/10.1175/2009JAS2883.1.

Bechini, R., L. Baldini, R. Cremonini, and E. Gorgucci, 2008: Differential reflectivity calibration for operational radars. *J. Atmos. Oceanic Technol.*, **25**, 1542–1555, https://doi.org/10.1175/2008JTECHA1037.1.

Bernstein, B. C., 2000: Regional and local influences on freezing drizzle, freezing rain, and ice pellet events. *Wea. Forecasting*, **15**, 485–508, https://doi.org/10.1175/1520-0434(2000)015<0485:RALIOF>2.0.CO;2.

——, T. Omeron, F. McDonough, and M. K. Polotovich, 1997: The relationship between aircraft icing and synoptic-scale weather conditions. *Wea. Forecasting*, **12**, 742–762, https://doi.org/10.1175/1520-0434(1997)012<0742:TRBAIA>2.0.CO;2.

Brown, B., G. Thompson, R. Bruintjes, R. Bullock, and T. Kane, 1997: Intercomparison of in-flight icing algorithms. Part II: Statistical verification results. *Wea. Forecasting*, **12**, 890–914, https://doi.org/10.1175/1520-0434(1997)012<0890:IOIFIA>2.0.CO;2.

Cao, Q., G. Zhang, E. A. Brandes, and T. J. Schuur, 2010: Polarimetric radar rain estimation through retrieval of drop size distribution using a Bayesian approach. *J. Appl. Meteor. Climatol.*, **49**, 973–990, https://doi.org/10.1175/2009JAMC2227.1.

——, ——, and M. Xue, 2013: A variational approach for retrieving raindrop size distribution from polarimetric radar measurements in the presence of attenuation. *J. Appl. Meteor. Climatol.*, **52**, 169–185, https://doi.org/10.1175/JAMC-D-12-0101.1.

Changnon, S. A., 2003: Urban modification of freezing-rain events. *J. Appl. Meteor.*, **42**, 863–870, https://doi.org/10.1175/1520-0450(2003)042<0863:UMOFE>2.0.CO;2.

Cho, J. Y. N., 2010: OEP terminal and CONUS weather radar coverage gap identification analysis for NextGen. MIT Lincoln Laboratory Project Rep. ATC-369, 93 pp., https://www.ll.mit.edu/sites/default/files/publication/doc/2018-09/Cho_2010_ATC-369_WW-20740.pdf.

Chrisman, J. N., 2009: Automated Volume Scan Evaluation and Termination (AVSET): A simple technique to achieve faster volume scan updates. *34th Conf. on Radar Meteorology*, Williamsburg, VA, Amer. Meteor. Soc., P4.4, https://ams.confex.com/ams/pdfpapers/155324.pdf.

Cober, S. G., and G. A. Isaac, 2012: Characterization of aircraft icing environments with supercooled large drops for application to commercial aircraft certification. *J. Appl. Meteor.*, **51**, 265–284, https://doi.org/10.1175/JAMC-D-11-022.1.

Cortinas, J. V., Jr., 2000: A climatology of freezing rain in the Great Lakes region of North America. *Mon. Wea. Rev.*, **128**, 3574–3588, https://doi.org/10.1175/1520-0493(2001)129<3574:ACOFRI>2.0.CO;2.

——, B. C. Bernstein, C. C. Robbins, and J. W. Strapp, 2004: An analysis of freezing rain, freezing drizzle, and ice pellets across the United States and Canada: 1976–1990. *Wea. Forecasting*, **19**, 377–390, https://doi.org/10.1175/1520-0434(2004)019<0377:AAOFRF>2.0.CO;2.

Crawford, R. W., and R. E. Stewart, 1995: Precipitation type characteristics at the surface in winter storms. *Cold Reg. Sci. Technol.*, **23**, 215–229, https://doi.org/10.1016/0165-232X(94)00014-O.

Dai, A., 2008: Temperature and pressure dependence of the rain-snow phase transition over land and ocean. *Geophys. Res. Lett.*, **35**, L12802, https://doi.org/10.1029/2008GL033456.

DiVito, S., and J. T. Riley, 2017: An overview of the Federal Aviation Administration (FAA) terminal area icing weather information for NextGen (TAIWIN) project. *18th Conf. on Aviation, Range, and Aerospace Meteorology*, Seattle, WA, Amer. Meteor. Soc., 7.1, https://ams.confex.com/ams/97Annual/webprogram/Paper314380.html.

Doviak, R. J., and D. S. Zrnić, 1993: *Doppler Radar and Weather Observations.* 2nd ed. Academic Press, 562 pp.

Ellrod, G. P., and A. A. Bailey, 2007: Assessment of aircraft icing potential and maximum icing altitude from geostationary meteorological satellite data. *Wea. Forecasting*, **22**, 160–174, https://doi.org/10.1175/WAF984.1.

Elmore, K. L., H. Grams, D. Apps, and H. Reeves, 2015: Verifying forecast precipitation type with mPING. *Wea. Forecasting*, **30**, 656–667, https://doi.org/10.1175/WAF-D-14-00068.1.

Federal Aviation Administration, 2015: Airplane and engine certification requirements in supercooled large drop, mixed phase, and ice crystal icing conditions; final rule. Parts 25 and 33, Aeronautics and Space, U.S. Code of Federal Regulations, National Archives and Records Administration, 34 pp., https://www.govinfo.gov/content/pkg/FR-2014-11-04/pdf/2014-25789.pdf.

Field, P. R., R. J. Hogan, P. R. A. Brown, A. J. Illingworth, T. W. Choularton, P. H. Kaye, E. Hirst, and R. Greenaway, 2004: Simultaneous radar and aircraft observations of mixed-phase cloud at the 100 m scale. *Quart. J. Roy. Meteor. Soc.*, **130**, 1877–1904, https://doi.org/10.1256/qj.03.102.

Giangrande, S. E., and A. V. Ryzhkov, 2003: The quality of rainfall estimation with the polarimetric WSR-88D radar as a function of range. *31st Int. Conf. on Radar Meteorology*, Seattle, WA, Amer. Meteor. Soc., 5B.5, https://ams.confex.com/ams/pdfpapers/64220.pdf.

——, ——, and J. Krause, 2005: Automatic detection of the melting layer with a polarimetric prototype of the WSR-88D radar. *32nd Conf. on Radar Meteorology*, Albuquerque, NM, Amer. Meteor. Soc., 11R.2, https://ams.confex.com/ams/pdfpapers/95894.pdf.

Hallowell, R. G., M. F. Donovan, D. J. Smalley, and B. J. Bennett, 2013: Icing hazard detection with NEXRAD IHL. *36th Conf. on Radar Meteorology*, Breckenridge, CO, Amer. Meteor. Soc., 263, https://ams.confex.com/ams/36Radar/webprogram/Manuscript/Paper228656/Hallowell_36RADAR_AMS.pdf.

Hanesiak, J. M., and R. E. Stewart, 1995: The mesoscale and microscale structure of a severe ice pellet storm. *Mon. Wea. Rev.*, **123**, 3144–3162, https://doi.org/10.1175/1520-0493(1995)123<3144:TMAMSO>2.0.CO;2.

Hudak, D., B. Currie, P. Rodreguez, S. G. Cober, I. Zawadzki, G. A. Isaac, and M. Wolde, 2002: Cloud phase detection in winter stratiform clouds using polarimetric Doppler radar. *Proc. Second European Conf. on Radar Meteorology*, Delft, Netherlands, Conernicus GmbH, 90–94.

Ice, R. L., G. T. McGehee, R. Rhoton, D. Saxion, D. A. Warde, R. G. Guenther, D. Sirmans, and D. Rachel, 2005: Radar Operations Center (ROC): Evaluation of new signal processing techniques for the WSR-88D. *21st Int. Conf. on Interactive Information Processing Systems for Meteorology, Oceanography, and Hydrology*, San Diego, CA, Amer. Meteor. Soc., P1.4, https://ams.confex.com/ams/pdfpapers/85859.pdf.

Kienzle, S. W., 2008: A new temperature based method to separate rain and snow. *Hydrol. Processes*, **22**, 5067–5085, https://doi.org/10.1002/hyp.7131.

Kumjian, M. R., 2013a: Principles and applications of dual-polarization weather radar. Part I: Description of the polarimetric radar variables. *J. Oper. Meteor.*, **1**, 226–242.

——, 2013b: Principles and applications of dual-polarization weather radar. Part II: Warm and cold season applications. *J. Oper. Meteor.*, **1**, 243–264.

——, A. V. Ryzhkov, H. D. Reeves, and T. J. Schuur, 2013: A dual-polarization radar signature of hydrometeor refreezing in winter storms. *J. Appl. Meteor. Climatol.*, **52**, 2549–2566, https://doi.org/10.1175/JAMC-D-12-0311.1.

Lakshmanan, V., T. Smith, K. Hondl, G. J. Stumpf, and A. Witt, 2006: A real-time, three-dimensional, rapidly updating, heterogeneous radar merger technique for reflectivity, velocity, and derived products. *Wea. Forecasting*, **21**, 802–823, https://doi.org/10.1175/WAF942.1.

Landolt, S. D., A. J. Schwartz, A. Gaydos, and S. DiVito, 2017: Impacts of the implementation of the Automated Surface Observing Station (ASOS) on the reports of precipitation type in airport terminal areas around the United States. *18th Conf. on Aviation, Range, and Aerospace Meteorology*, Seattle, WA, Amer. Meteor. Soc., 8.4, https://ams.confex.com/ams/97Annual/webprogram/Paper313277.html.

Meyers, M. P., P. J. DeMott, and W. R. Cotton, 1992: New primary ice-nucleation parameterization in an explicit cloud model. *J. Appl. Meteor.*, **31**, 708–721, https://doi.org/10.1175/1520-0450(1992)031<0708:NPINPI>2.0.CO;2.

Motoyama, H., 1990: Simulation of seasonal snow cover based on air temperature and precipitation. *J. Appl. Meteor.*, **29**, 1104–1110, https://doi.org/10.1175/1520-0450(1990)029<1104:SOSSBO>2.0.CO;2.

NOAA, 1998: Automated Surface Observing System (ASOS) user's guide. National Oceanic and Atmospheric Administration, 67 pp., https://www.weather.gov/media/asos/aum-toc.pdf.

Park, H.-S., A. V. Ryzhkov, D. S. Zrnić, and K.-E. Kim, 2009: The hydrometeor classification algorithm for the polarimetric WSR-88D: Description and application to an MCS. *Wea. Forecasting*, **24**, 730–748, https://doi.org/10.1175/2008WAF2222205.1.

Petters, M. D., and T. P. Wright, 2015: Revisiting ice nucleation from precipitation samples. *Geophys. Res. Lett.*, **42**, 8758–8766, https://doi.org/10.1002/2015GL065733.

Plummer, D. M., S. Göke, R. M. Rauber, and L. DiGirolamo, 2010: Discrimination of mixed- versus ice-phase clouds using dual-polarized radar with application to detection of aircraft icing regions. *J. Appl. Meteor. Climatol.*, **49**, 920–936, https://doi.org/10.1175/2009JAMC2267.1.

Politovich, M. K., and B. C. Bernstein, 1995: Production and depletion of supercooled liquid water in a Colorado winter storm. *J. Appl. Meteor.*, **34**, 2631–2648, https://doi.org/10.1175/1520-0450(1995)034<2631:PADOSL>2.0.CO;2.

Radar Operations Center, 2015: WSR-88D volume coverage patterns improvement initiatives. NOAA, 8 pp., https://www.roc.noaa.gov/WSR88D/PublicDocs/NewTechnology/New_VCP_Paradigm_Public_Oct_2015.pdf.

Rauber, R. M., L. S. Olthoff, and M. K. Ramamurthy, 2000: The relative importance of warm rain and melting processes in freezing precipitation events. *J. Appl. Meteor.*, **39**, 1185–1195, https://doi.org/10.1175/1520-0450(2000)039<1185:TRIOWR>2.0.CO;2.

——, ——, ——, and K. E. Kunkel, 2001: Further investigation of a physically based, nondimensional parameter for discriminating between locations of freezing rain and ice pellets. *Wea. Forecasting*, **16**, 185–191, https://doi.org/10.1175/1520-0434(2001)016<0185:FIOAPB>2.0.CO;2.

Reeves, H. D., 2016: The uncertainty of precipitation-type observations and its effect on the validation of forecast precipitation type. *Wea. Forecasting*, **31**, 1961–1971, https://doi.org/10.1175/WAF-D-16-0068.1.

——, K. L. Elmore, A. Ryzhkov, T. Schuur, and J. Krause, 2014: Source of uncertainty in precipitation-type forecasting. *Wea. Forecasting*, **29**, 936–953, https://doi.org/10.1175/WAF-D-14-00007.1.

——, A. V. Ryzhkov, and J. Krause, 2016: Discrimination between winter precipitation types based on spectral-bin microphysical modeling. *J. Appl. Meteor. Climatol.*, **55**, 1747–1761, https://doi.org/10.1175/JAMC-D-16-0044.1.

Robbins, C. C., and J. V. Cortinas Jr., 2002: Local and synoptic environments associated with freezing rain in the contiguous United States. *Wea. Forecasting*, **17**, 47–65, https://doi.org/10.1175/1520-0434(2002)017<0047:LASEAW>2.0.CO;2.

Rohrer, M. D., 1989: Determination of the transition air temperature from snow and rain and intensity of precipitation. *IAHS/WMO/ETH Int. Workshop of Precipitation Measurement*, IAHS/WMO/ETH, St. Moritz, Switzerland, 475–482.

Ryzhkov, A. V., 2007: The impact of beam broadening on the quality of radar polarimetric data. *J. Atmos. Oceanic Technol.*, **24**, 729–744, https://doi.org/10.1175/JTECH2003.1.

——, D. S. Zrnić, J. C. Hubbert, V. N. Bringi, J. Vivekanandan, and E. A. Brandes, 2002: Polarimetric radar observations and interpretation of co-cross-polar correlation coefficients. *J. Atmos. Oceanic Technol.*, **19**, 340–354, https://doi.org/10.1175/1520-0426-19.3.340.

——, S. E. Giangrande, V. M. Melnikov, and T. J. Schuur, 2005a: Calibration issues of dual-polarization radar measurements. *J. Atmos. Oceanic Technol.*, **22**, 1138–1155, https://doi.org/10.1175/JTECH1772.1.

——, T. J. Schuur, D. W. Burgess, S. Giangrande, and D. S. Zrnić, 2005b: The Joint Polarization Experiment: Polarimetric rainfall measurements and hydrometeor classification. *Bull. Amer. Meteor. Soc.*, **86**, 809–824, https://doi.org/10.1175/BAMS-86-6-809.

——, P. Zhang, H. Reeves, M. Kumjian, T. Tschallener, S. Trömel, and C. Simmer, 2016: Quasi-vertical profiles—A new way to look at polarimetric radar data. *J. Atmos. Oceanic Technol.*, **33**, 551–562, https://doi.org/10.1175/JTECH-D-15-0020.1.

Serke, D., S. Ellis, J. Hubbert, D. Albo, C. Johnston, C. Coy, D. Adriaanson, and M. Politovich, 2013: In-flight icing hazard detection with dual and single-polarimetric moments from operational NEXRADs. *36th Conf. on Radar Meteorology*, Breckenridge, CO, Amer. Meteor. Soc., 15A.4, https://ams.confex.com/ams/36Radar/webprogram/Manuscript/Paper228592/AMSRAD_2013_extabs_v1%20%281%29.pdf.

Smith, T. M., and Coauthors, 2016: Multi-Radar Multi-Sensor (MRMS) severe weather and aviation products: Initial operating capabilities. *Bull. Amer. Meteor. Soc.*, **97**, 1617–1630, https://doi.org/10.1175/BAMS-D-14-00173.1.

Smith, W. L., Jr., P. Minnis, C. Fleeger, D. Spangenberg, R. Palikonda, and L. Nguyen, 2012: Determining the flight icing threat to aircraft with single-layer cloud parameters derived from operational satellite data. *J. Appl. Meteor. Climatol.*, **51**, 1794–1810, https://doi.org/10.1175/JAMC-D-12-057.1.

Tafferner, A., T. Hauf, C. Leifeld, T. Hafner, H. Leykauf, and U. Voigt, 2003: ADWICE: Advanced Diagnosis and Warning System for Aircraft Icing Environments. *Wea. Forecasting*, **18**, 184–203, https://doi.org/10.1175/1520-0434(2003)018<0184:AADAWS>2.0.CO;2.

Tang, L., J. Zhang, C. Langston, J. Krause, K. Howard, and V. Lakshmanan, 2014: A physically based precipitation–nonprecipitation radar echo classifier using polarimetric and environmental data in a real-time national system. *Wea. Forecasting*, **29**, 1106–1119, https://doi.org/10.1175/WAF-D-13-00072.1.

Thériault, J. M., R. E. Stewart, and W. Henson, 2010: On the dependence of winter precipitation types and temperature, precipitation rate, and associated features. *J. Appl. Meteor. Climatol.*, **49**, 1429–1442, https://doi.org/10.1175/2010JAMC2321.1.

Thompson, E. J., S. A. Rutledge, B. Dolan, V. Chandrasekar, and B.-L. Cheong, 2014: A dual-polarized radar hydrometeor classification algorithm for winter precipitation. *J. Atmos. Oceanic Technol.*, **31**, 1457–1481, https://doi.org/10.1175/JTECH-D-13-00119.1.

VanDenBroeke, M. S., D. M. Tobin, and M. R. Kumjian, 2016: Polarimetric radar observations of precipitation type and rate from the 2–3 March 2014 winter storm in Oklahoma. *Wea. Forecasting*, **31**, 1179–1196, https://doi.org/10.1175/WAF-D-16-0011.1.

Wolde, M., D. Hudak, B. Currie, S. G. Cober, P. Rodriguez, I. Zawadzki, G. A. Isaac, and D. Marcotte, 2003: Radar signatures of winter clouds from aircraft in-situ data and ground-based radar observations. *31st Conf. on Radar Meteorology*,

Seattle, WA, Amer. Meteor. Soc., 13.3, https://ams.confex.com/ams/pdfpapers/64348.pdf.

Yang, Z. L., R. E. Dickinson, A. Robock, and K. Y. Vinnikov, 1997: Validation of the snow submodel of the biosphere–atmosphere transfer scheme with Russian snow cover and meteorological observational data. *J. Climate*, **10**, 353–373, https://doi.org/10.1175/1520-0442(1997)010<0353:VOTSSO>2.0.CO;2.

Yoshikawa, E., V. Chandrasekar, and T. Matsuda, 2014: Raindrop size distribution (DSD) retrieval for X-band dual-polarization radar. *J. Atmos. Oceanic Technol.*, **31**, 387–403, https://doi.org/10.1175/JTECH-D-12-00248.1.

Zhang, J., and Coauthors, 2016: Multi-Radar Multi-Sensor (MRMS) quantitative precipitation estimation: Initial operating capabilities. *Bull. Amer. Meteor. Soc.*, **97**, 621–638, https://doi.org/10.1175/BAMS-D-14-00174.1.